ADVANCED FUNCTIONAL MATERIALS
www.afm-journal.de

Distinctive Doping Behavior of Conjugated Polymers With Pendant-Side Conjugation for Enhanced Thermoelectric Properties

Hyeokjun Kim, Sang Beom Kim, Seungok Pyo, Jaeyoung Jang, and In Hwan Jung**

Organic thermoelectric (OTE) materials are continuously evolving through the development of novel conjugated polymers and corresponding doping methods. $FeCl_3$ doping is the most commonly used method because of its affordability and strong oxidizing power. However, at high dopant concentrations, $FeCl_3$ interferes with the molecular ordering and negatively impacts on the morphology, which causes a substantial decline in performance. To address this issue, in this study, new OTE polymers with π-conjugation along the pendant side are developed. This unique polymeric structure enables pendant doping with $FeCl_3$ by forming a strong binding complex at the conjugated side chains, where an abundant free volume exists. Consequently, the intermolecular ordering of the OTE polymer is well preserved even under high dopant concentration, thereby enabling a high power factor exceeding 10 μW m^{-1} K^{-2} consistently across a wide range of high dopant concentrations (16–32 mM) for the first time. This distinctive doping behavior on the pendant side will provide a new opportunity to develop high-performance OTE polymers.

1. Introduction

As modern technologies come closer to human interfaces,[1–5] the demand for flexible[6–8] and attachable[9–11] materials has gradually increased to realize portable[12–14] and wearable[15–17] devices. Organic thermoelectric (OTE) devices are one of the most promising energy harvesting devices for wearable gadgets because it can directly convert human body heat to electricity, which can be considered as a semi-permanent power supply.[18–22] Typically, TE performance is defined as $ZT = S^2\sigma T/\kappa$, where S is the Seebeck coefficient, σ is the electrical conductivity, T is the absolute temperature, and κ is the thermal conductivity.[23–30] Because of the low value of κ in organic conjugated materials,[31] most of the efforts to improve TE performance have been focused on increasing the S and σ values. This is collectively reflected in the power factor (PF), which is expressed as PF $= S^2\sigma$, and elevating the PF becomes a crucial metric to enhance the OTE performance. However, because organic conjugated materials have intrinsically low σ, the chemical doping on the OTE materials is fundamental to achieve good OTE performance.[32–35] One of the well-developed doping systems is using $FeCl_3$ as a p-type dopant,[36–39] which shows unique advantages of low-cost, good solubility in common organic solvents, efficient diffusion into the polymer films, and strong oxidizing characteristics. Geng et al. reported novel ambipolar OTE polymers through immersion doping of dilute $FeCl_3$ solution (5 mM), which demonstrated a promising σ of 168 S cm^{-1}, a S of 118.9 μV K^{-1}, and a PF of 237.5 μW m^{-1} K^{-2}.[40] Ding et al. reported benzothiadiazole-based p-type OTE polymers with varying alkyl side chains using immersion doping of dilute $FeCl_3$ solution (6 mM) and achieved a high σ of 118.7 S cm^{-1}, a S of 43.5 μV K^{-1}, and a PF of 22.4 μW m^{-1} K^{-2}.[41] Suh et al. reported cyclopentadithiophene (CPDT)-based OTE polymer with a shallow highest occupied molecular orbital (HOMO) energy level through the sequential spin coating of low-concentration $FeCl_3$ solution (6 mM), which resulted in a σ of 0.91 S cm^{-1}, a S of 32 μV K^{-1}, and a PF of 0.1 μW m^{-1} K^{-2}.[42] Liu et al. reported diketopyrrolopyrrole-based OTE polymer containing ethylenedioxythiophene building blocks using the sequential spin coating of very low-concentration $FeCl_3$ solution (0.5 mM), which exhibited a highly promising σ of 99.2 S cm^{-1}, S of 174.2 μV K^{-1}, and PF of 298.2 μW m^{-1} K^{-2}.[43] Although numerous OTE polymers have demonstrated high TE performance through $FeCl_3$ doping, a significant issue remains: at high concentrations of $FeCl_3$, the OTE performance decreases remarkably because the $FeCl_4^-$ counter anion acts as an impurity, which disrupts the π-π stacking ordering of the OTE polymers and compromises the doping stability.[44–50] Therefore, the development of OTE

H. Kim, S. Pyo, I. H. Jung
Department of Organic and Nano Engineering, and Human-Tech Convergence Program
Hanyang University
222 Wangsimni-ro, Seongdong-gu, Seoul 04763, Republic of Korea
E-mail: inhjung@hanyang.ac.kr

S. B. Kim, J. Jang
Department of Energy Engineering
Hanyang University
222 Wangsimni-ro, Seongdong-gu, Seoul 04763, Republic of Korea
E-mail: jyjang15@hanyang.ac.kr

The ORCID identification number(s) for the author(s) of this article can be found under https://doi.org/10.1002/adfm.202422778

DOI: 10.1002/adfm.202422778

polymers that can maintain high performances at high dopant concentration is important to address this problem in the $FeCl_3$ doping system.

In this study, novel OTE polymers capable of maintaining an ordered polymeric architecture even under heavy doping of $FeCl_3$ were designed by promoting pendant doping. Accordingly, a novel electron-withdrawing building block, dibrominated 2-(thieno[3,4-*b*]thiophen-2-ylmethylene)malononitrile (TTMN), was synthesized and incorporated into a polymeric backbone structure to promote pendant doping. TTMN has a strong electron-withdrawing malononitrile functional group at the end of the thieno[3,4-*b*]thiophene, which increases the electron density and dipole moment toward the pendant side of the polymer when it is incorporated into the polymer chain. We believe that this unique molecular structure of TTMN can improve the π-conjugation of the polymers along the pendant side and form a strong binding complex with $FeCl_4^-$ counter anions at the pendant side where abundant free volume exists. Therefore, pendant doping is considered an effective method for high-concentration $FeCl_3$ doping without disrupting the molecular ordering of the polymer chains.

To build TTMN-based OTE polymers, three building blocks, 4*H*-cyclopenta[2,1-*b*:3,4-*b*″]dithiophene (CPDT), benzo[1,2-*b*:4,5-*b*″]dithiophene (BDT), and indaceno[1,2-*b*:5,6-*b*″]dithiophene (IDT), which have different electron-donating strengths, were copolymerized with TTMN through the Stille coupling reaction, and three novel OTE polymers, poly[(4,4-bis(2-ethylhexyl)-4*H*-cyclopenta[2,1-*b*:3,4-*b*″]dithiophene-2,6-diyl)-*alt*-(2-(thieno[3,4-*b*]thiophen-2-ylmethylene)malononitrile-4,6-diyl)] (PTMN1), poly[(4,8-bis(5-(2-ethylhexyl)thiophen-2-yl)benzo[1,2-*b*:4,5-*b*″]dithiophene-2,6-diyl)-*alt*-(2-(thieno[3,4-*b*]thiophen-2-ylmethylene)malononitrile-4,6-diyl)] (PTMN2), and poly[(4,4,9,9-tetrakis(4-hexylphenyl)-4,9-dihydro-*s*-indaceno[1,2-*b*:5,6-*b*″]dithiophene-2,7-diyl-*alt*-(2-(thieno[3,4-b]thiophen-2-ylmethylene)malononitrile-4,6-diyl)] (PTMN3), were synthesized, respectively. All the synthesized polymers had an alternating donor-acceptor (D-A) backbone structure with identical TTMN A moieties and varying electron-donating strengths. The stronger electron-donating strength intensified the π-conjugation and π-bond delocalization along the conjugated polymer backbone, which favored backbone doping with $FeCl_3$ (PTMN1). In contrast, the weaker electron-donating moiety could not facilitate efficient backbone conjugation. As an alternative, pendant doping at the end of the TTMN moiety was activated in PTMN2. Notably, the intermolecular ordering of PTMN1 was significantly decreased by backbone doping with $FeCl_3$, which resulted in low σ and PF at high dopant concentrations. Conversely, the intermolecular ordering of PTMN2 was well preserved even under high-concentration doping owing to pendant doping with $FeCl_3$, which resulted in the highest σ and S. The PF of PTMN2 reached 12.8 μW m^{-1} K^{-2}, which was 44 times higher than that of PTMN1 (0.29 μW m^{-1} K^{-2}). Interestingly, the high PF value of PTMN2 was not just a singular occurrence; rather, the high PF values exceeding 10 μW m^{-1} K^{-2} were consistently maintained across a broad range of dopant concentrations (16–32 mM). The preferred pendant doping in PTMN2 improved the OTE performances at high dopant concentrations because $FeCl_4^-$ counter anions were captured at the end of the TTMN moiety, which minimized morphological disorder of the polymers under the doped states.

2. Results and Discussion

2.1. Synthesis and Characterization

A novel **TTMN** building block, which incorporates strong electron-withdrawing malononitrile groups at the pendant position of TTe, was synthesized as depicted in **Scheme 1**. Compound 1 was synthesized by the formylation of 3,4-dibromothiophene using dimethylformamide through a lithium-halogen exchange reaction, which was subsequently subjected to a ring-closing reaction with ethyl thioglycolate to obtain compound 2. Compound 3 was synthesized by reducing compound 2 using a lithium aluminum hydroxide ($LiAlH_4$) solution, and this compound was conducted oxidation to aldehyde using pyridinium chlorochromate (PCC) to obtain compound 4. TTMN was synthesized through activated aluminum oxide-assisted Knoevenagel condensation between malononitrile and compound 4, as previously reported.[51] The final monomer, compound 5, was obtained by the dibromination of TTMN using two equivalents of *N*-bromosuccinimide (NBS). To synthesize novel OTE polymers based on TTMN, three different stannylated comonomers (4,4-bis(2-butyloctyl)-4*H*-cyclopenta[2,1-*b*:3,4-*b*″]dithiophene-2,6-diyl)bis(trimethylstannane) (**CPDT**), (4,8-bis(5-(2-ethylhexyl)thiophen-2-yl)benzo[1,2-*b*:4,5-*b*″]dithiophene-2,6-diyl)bis(trimethylstannane) (**BDT**), (4,4,9,9-tetrakis(4-hexylphenyl)-4,9-dihydro-s-indaceno[1,2-*b*:5,6-*b*′]dithiophene-2,7-diyl)bis(trimethylstannane) (**IDT**), were copolymerized with the dibrominated TTMN (compound 5) through microwave-assisted Stille polymerization, which yielded the final OTE copolymers named PTMN1, PTMN2, and PTMN3, respectively. All polymers demonstrated sufficient solubility in common organic solvents such as methylene chloride, chloroform, and tetrahydrofuran. The molecular weights of the OTE polymers were evaluated by gel permeation chromatography (GPC); the average molecular weights (M_n) of PTMN1, PTMN2, and PTMN3 were 9.3, 4.6, and 6.5 kDa, respectively, and the weight-average molecular weights (M_w) were 14.8, 11.0, and 11.2 kDa, respectively. All the synthesized monomers and polymers were identified using ^{1}H NMR spectroscopy, and the detailed characterization results are described in Supporting Information.

The optical properties were investigated by UV–Vis spectroscopy, both in chloroform solution and in the film state **Figure** (1a,b). The maximum absorption peak (λ_{max}) of PTMN1, PTMN2, and PTMN3 in solution state appeared at 844, 696, and 728 nm, respectively. Because all the polymers had D-A type conjugated backbone structure, the degree of intramolecular charge transfer (ICT) interactions between the electron-donating building blocks (CPDT, BDT, and IDT) and electron-withdrawing TTMN directly influenced the extent of the bathochromic shift in the absorption peak. PTMN1, which had the strongest electron-donating CPDT moiety, exhibited the most red-shifted absorption compared to the other polymers, which indicates a strongest ICT interaction in PTMN1. The absorption behaviors of PTMN2 and PTMN3 were similar, indicating a similar degree of ICT interaction. Interestingly, in the film states, the λ_{max} of PTMN2 strongly red-shifted from 696 to 711 nm, while that of PTMN1

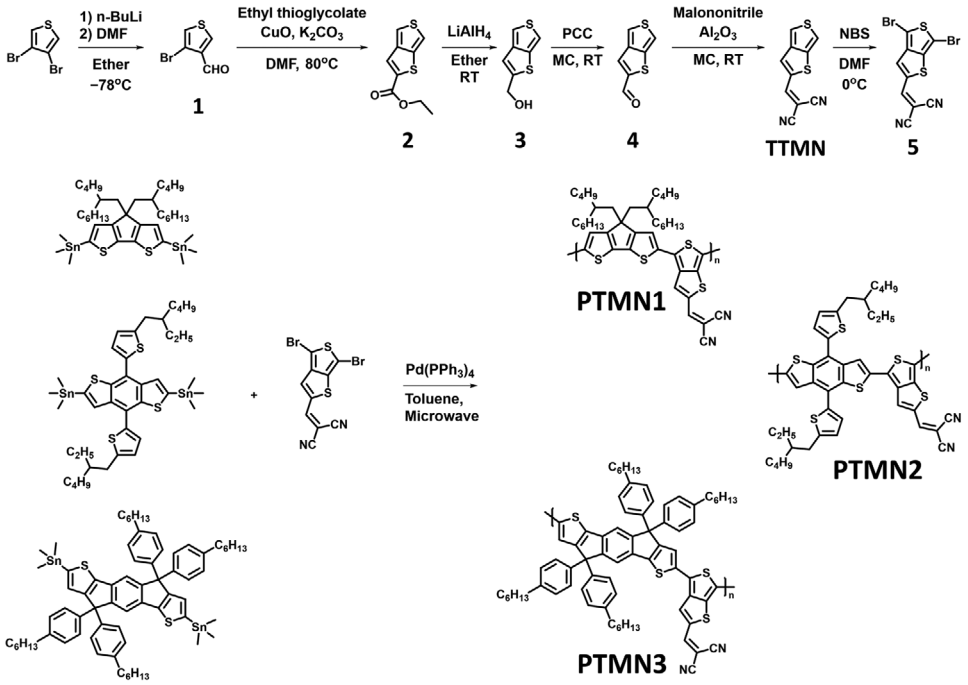

Scheme 1. Synthesis of thieno[3,4-*b*]thiophene derivative monomers and OTE polymers.

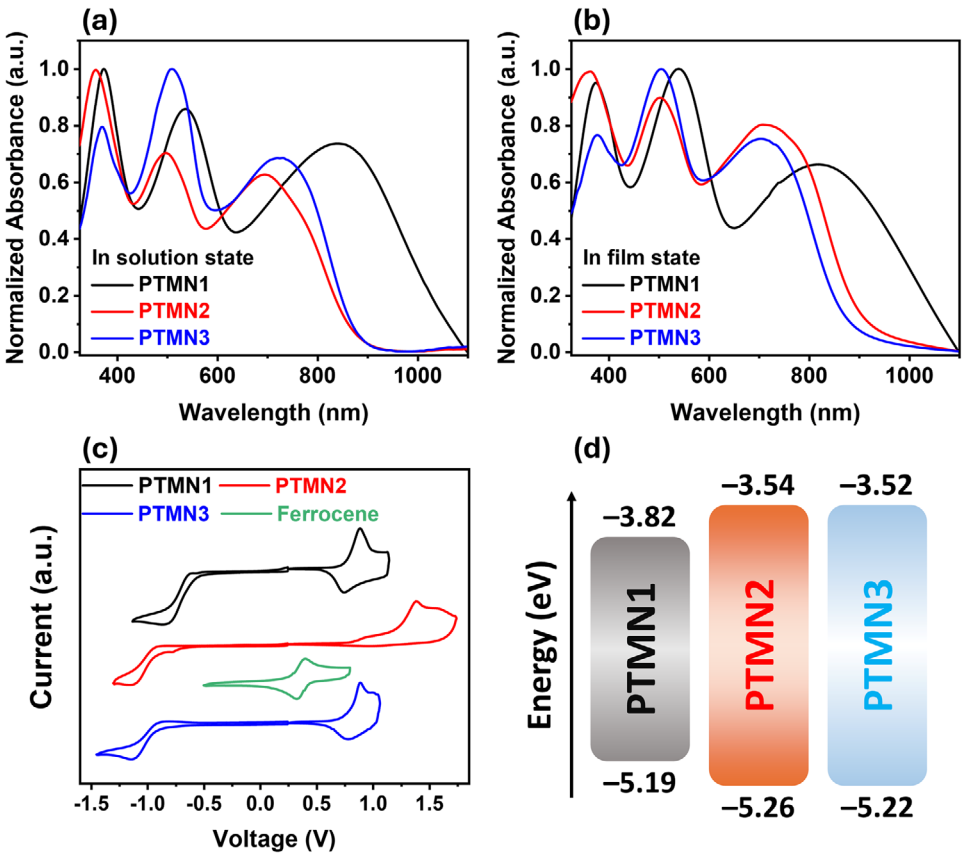

Figure 1. UV–vis absorption spectrum of OTE polymers a) in solution and b) in film state. c) Cyclic voltammograms of OTE polymers and d) energy level diagrams of OTE polymers in neutral state.

Table 1. Summary of optical and electrochemical properties.

	λ_{max} [nm]		λ_{onset} [nm]	E_g^{Opt} [eV]	Onset potential [V]			E_{HOMO} [eV]	E_{LUMO} [eV]
	Solution	Film			E_{ox}	E_{re}	E_{ferr}		
PTMN1	844, 539, 373	821, 539, 375	1144	1.08	0.76	−0.61	0.37	−5.19	−3.82
PTMN2	696, 497, 356	711, 503, 365	960	1.29	0.83	−0.89	0.37	−5.26	−3.54
PTMN3	728, 509, 369	705, 504, 378	917	1.35	0.79	−0.91	0.37	−5.22	−3.52

and PTMN3 experienced a blue-shift from 844 to 821 nm and from 728 to 705 nm, respectively. This indicates that the intermolecular interactions of PTMN2 were improved in the film state, whereas those of PTMN1 and PTMN3 were weakened in the film state. PTMN2 has a more favorable structure for intermolecular ordering. The optical bandgap (E_g^{Opt}) of PTMN1, PTMN2, and PTMN3 evaluated from the thin-film absorption onset wavelength (λ_{onset}) was 1.08, 1.29, and 1.35 eV, respectively. Owing to the strong electron-withdrawing properties of TTMN, all the OTE polymers exhibited a low bandgap of less than 1.4 eV. However, PTMN1 exhibited an extremely low bandgap, almost close to ≈1 eV, implying highly efficient π-conjugation along the conjugated polymer backbone. This characteristic is favorable for backbone doping with $FeCl_3$.

The HOMO and lowest unoccupied molecular orbital (LUMO) energy levels were estimated by cyclic voltammetry (CV) based on the oxidation (E_{ox}) and reduction (E_{re}) onset potentials, respectively (Figure 1c). The E_{ox} of PTMN1, PTMN2 and PTMN3 were 0.76, 0.83, and 0.79 V, respectively, corresponding to the HOMO energy levels of −5.19, −5.26, and −5.22 eV, respectively. As shown in Figure 1d, the HOMO energy level of PTMN1 was higher than those of PTMN2 and PTMN3 because of the strong electron-donating properties of the CPDT building block. The E_{re} of PTMN1, PTMN2, and PTMN3 were −0.61, −0.89, and −0.91 V, respectively, corresponding to the LUMO energy levels of −3.82, −3.54, and −3.52 eV, respectively. Given that all the polymers shared an identical electron-withdrawing TTMN moiety, the low-lying LUMO energy level of PTMN1 suggests an effective π-conjugation between the CPDT and TTMN moieties, which was facilitated by their strong ICT interaction. The electrochemical bandgap (E_g^{CV}) of PTMN1, PTMN2, and PTMN3 was calculated to be −1.37, −1.72, and −1.70 eV, respectively. E_g^{CV} exhibited a trend similar to E_g^{Opt}: PTMN1 had a lower bandgap than PTMN2 and PTMN3, whereas PTMN2 and PTMN3 had similar bandgaps. The optical and electrochemical properties of the OTE polymers are summarized in **Table 1**.

2.2. Doping Characteristics

Doping is essential to increase the σ value of intrinsically non-conductive conjugated polymers. The doping characteristics of the OTE polymers were investigated using UV–Vis–NIR spectroscopy as a function of the $FeCl_3$ dopant concentration (**Figure 2a–d**). As the dopant concentration increased, the absorption peak ≈500 nm (ICT band, non-doped state) gradually decreased, whereas that ≈1000–2500 nm (bipolaronic band, doped state) increased. This indicates that cationic charge carriers were successfully generated in the conjugated backbone by $FeCl_3$ p-doping. Interestingly, PTMN1 demonstrated different doping behaviors than PTMN2 and PTMN3. As shown in Figure 2a–c, after $FeCl_3$ doping, almost all the absorption peaks of PTMN1 in the neutral state disappeared; however, the polaron/bipolaron absorption substantially increased and manifested as a single prominent absorption peak in the range of 1000–2500 nm. However, for PTMN2 and PTMN3, although the intensities of the absorption peaks in the neutral state decreased as the dopant concentration increased, their shapes were retained during doping. Furthermore, the absorption of polarons at ≈1000 nm and bipolarons near 2500 nm was clearly distinguishable and gradually increased with the dopant concentration. This implies that PTMN1 underwent facile doping, which resulted in extensive charge delocalization along the conjugated polymer backbones, whereas PTMN2 and PTMN3 appeared to have relatively low doping efficiencies and a limited range of charge delocalization along the conjugated backbone. The doping efficiency was evaluated using a linear plot of the bipolaronic band (≈2500 nm) to the ICT band (≈500 nm) ratio in the region where the dopant concentration and this ratio maintain a linear relationship,[52] as shown in Figure 2d and Figure S16 (supporting Information). The bipolaronic-to-ICT absorption ratio (I_{2500}/I_{ICT}) of PTMN1 increased sharply with increasing dopant concentrations and eventually saturated at 4 mM. In contrast, the I_{2500}/I_{ICT} values of PTMN2 increased relatively slowly with increasing dopant concentrations and maintained linearity even at high dopant concentrations (32 mM). In the case of PTMN3, the I_{2500}/I_{ICT} ratio resembles that of PTMN2 at low dopant concentrations (0–6 mM), but beyond this range, it follows a trend similar to PTMN1, with the bipolaron peak gradually saturating. The slopes of the I_{2500}/I_{ICT} lines for PTMN1, PTMN2, and PTMN3 were 0.885 (0–4 mM), 0.021 (0–32 mM), and 0.139 (0–6 mM, 1st)/ 0.451 (6–16 mM, 2nd), respectively. This clearly indicates that the doping efficiency increased in the order PTMN1 > PTMN3 > PTMN2, and PTMN1 exhibited an outstanding doping efficiency compared to the others. The strong ICT interaction between CPDT and TTMN was key to improving the doping efficiency by promoting charge delocalization along the PTMN1 conjugated backbone.

The doping levels of the doped polymer films were also estimated using XPS analysis by measuring the oxidation and neutral states of sulfur in the polymer backbone, to calculate the ratios of neutral, polaron, and bipolaron states in the films. The S 2p peaks were fitted using a Gaussian-Lorentz sum mix and a simplex fitting algorithm.[53] Additionally, the formation of polaron and bipolaron leading to shift of the neutral component to higher binding energy by 0.7–0.8 and 2.0–2.1 eV, respectively.[54,55] Interestingly, oxide sulfur peaks (polaron and bipolaron) were observed even in the undoped films, with increasing their ratio in the order of PTMN2 (0.07/0.93 = 7.5 (%)),

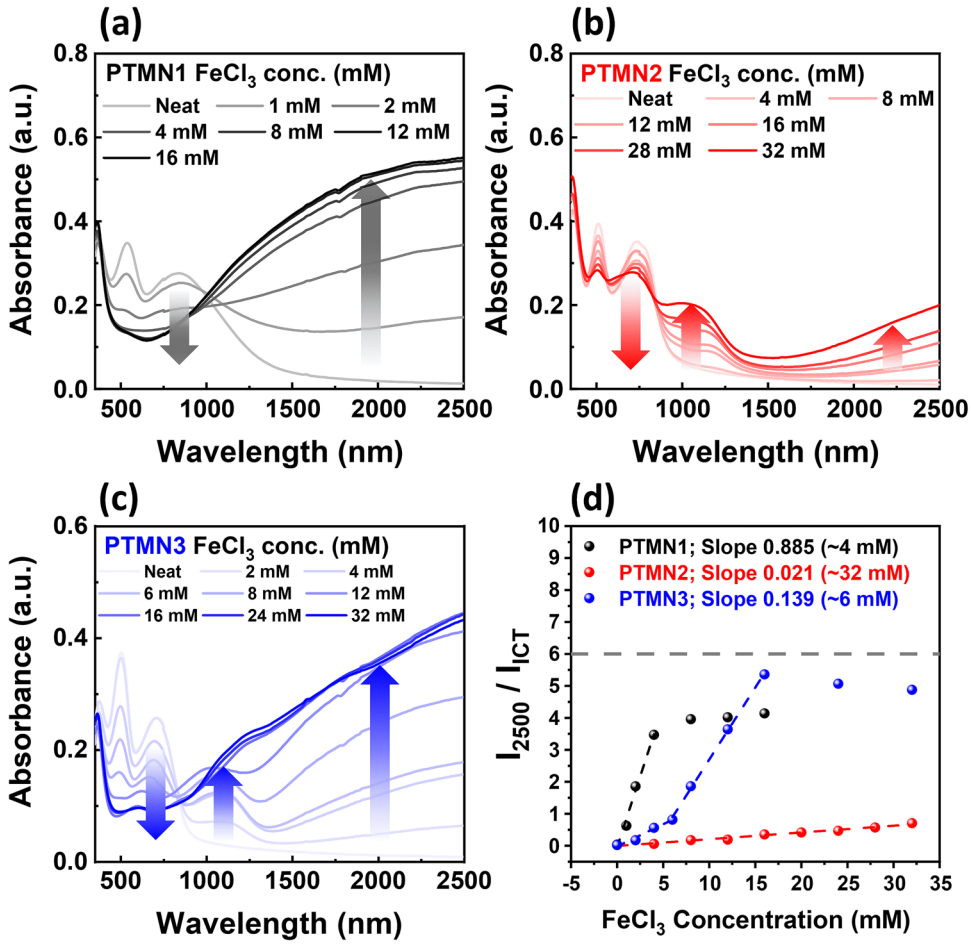

Figure 2. UV–vis-NIR absoroption spectra of OTE polymers as function of dopant concentration; a) PTMN1, b) PTMN2 and c) PTMN3. d) The bipolaronic peak (I_{2500}) to neutral peak (I_{ICT}) of PTMN1 (black line), PTMN2 (red line) and PTMN3 (blue line).

PTMN3 (0.04 × 2/0.96 = 8.3 (%)), and PTMN1 (0.07 × 2/0.93 = 15.1 (%)) (Figure S17a–c, Supporting Information). PTMN1–3 films were deposited on a gold layer, to prevent accumulated charges that cause binding energy shifts in XPS spectra. Since the work function of gold (5.1–5.4 eV) is deeper than the HOMO levels of the PTMN polymers (–5.19 to –5.26 eV), the oxide sulfur peaks (polaron and bipolaron) in the pristine films likely resulted from charge transfer between the gold contact electrode and the PTMN1–3 polymers.[56] As shown in Figure S17d–f (Supporting Information), the polaron and bipolaron peaks increased in $FeCl_3$-doped PTMN1–3 films, with a remarkable increase in these peaks for $FeCl_3$-doped PTMN1 and PTMN3 compared to PTMN2. Additionally, the precise doping levels, calculated from the ratios of polaron and bipolaron states to neutral states, are as follows: PTMN1 ((0.14 × 2+0.11)/0.75 = 52.0 (%)), PTMN2 ((0.05 × 2+0.05)/0.9 = 16.7 (%)), and PTMN3 ((0.07 × 2+0.20)/0.75 = 45.9 (%)) (Figure S17g–i, Supporting Information). These results are consistent with the UV–Vis–NIR data presented in Figure 2.

2.3. Thermoelectric Properties

First, σ of PTMN1–3 films were optimized as a function of annealing temperature while keeping the $FeCl_3$ concentration constant (Figure S18, Supporting Information). PTMN2 exhibited a 1-order increase in σ with increasing annealing temperature, whereas PTMN1 and PTMN3 maintained relatively constant σ. This is probably due to the significant improvement in molecular ordering with increasing annealing temperature in PTMN2, in contrast to the minimal changes in PTMN1 and PTMN3 after thermal annealing.

Next, an OTE device was fabricated to measure the TE performance of the OTE polymers with varying $FeCl_3$ dopant concentrations (**Figure 3a–d**) and the film thickness information were shown in Figure S19 (Supporting Information). As shown in Figure 3b, PTMN1 exhibited a high σ value of 1.3×10^{-2} S cm^{-1} in the lightly-doped state. In contrast, PTMN3 began to show σ of 6.0×10^{-3} S cm^{-1} at 2 mM dopant concentration, and PTMN2 started to show σ of 1.0×10^{-3} S cm^{-1} even at higher dopant concentration (4 mM). This clearly implies that the higher the doping efficiency of the OTE polymers, the lower the dopant concentration required to establish σ. Very interestingly, the σ of PTMN1 saturated early at lower dopant concentrations (4 mM) owing to its high doping efficiency; however, its maximum value remained low at a level of 0.15 S cm^{-1}. Conversely, PTMN2 demonstrated a gradual increase in σ relative to the dopant concentration, which was attributed to its lower doping efficiency. However, it achieved

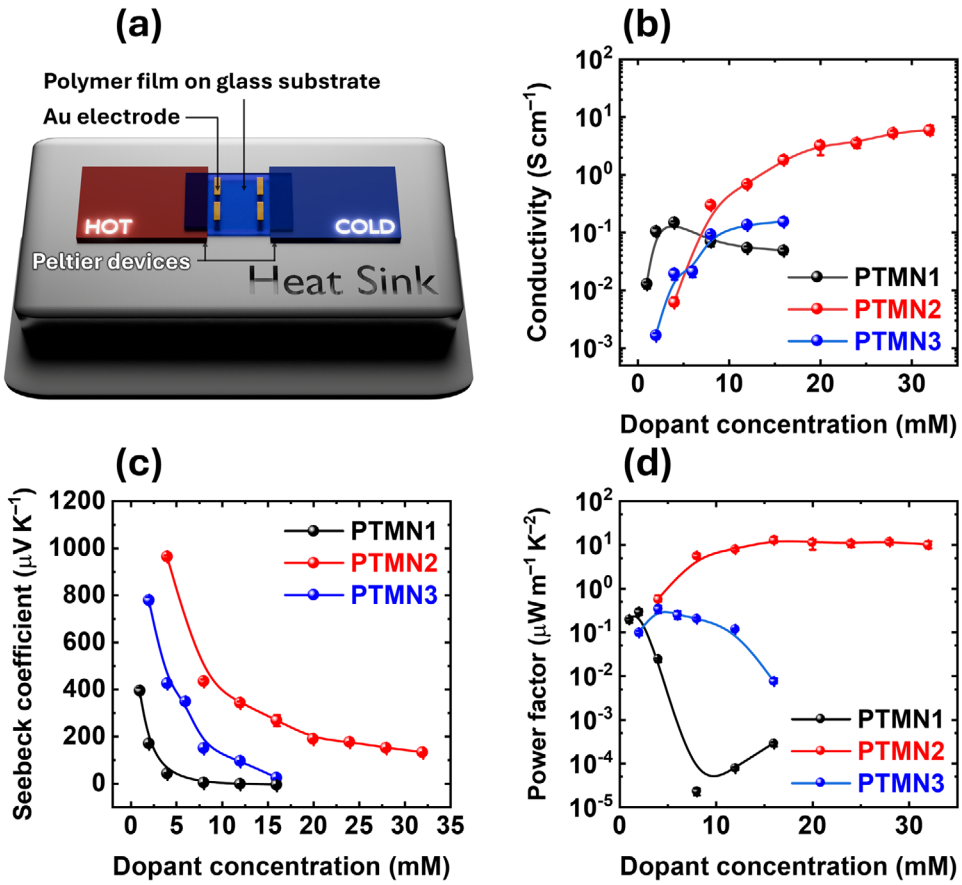

Figure 3. a) Schematic illustration of thermoelectric device and thermoelectric performance of annealed OTE polymers; b) Electrical conductivity, c) Seebeck coefficient, and d) power factor.

an exceptionally high σ of 5.9 S cm^{-1} at much higher dopant concentrations (32 mM). In the case of PTMN3, the σ curve exhibited a trend between those of PTMN1 and PTMN2.

Given that all three OTE polymers exhibited a similar molecular structure based on TTMN, the remarkably different trends in σ are not only intriguing but also suggest the presence of distinct doping mechanisms among PTMN1–3. Doping with OTE polymers induced a positive charge on the conjugated backbone, which was stabilized by delocalization along the conjugated backbone. Therefore, understanding how the cationic charge carrier stabilizes in a conjugated backbone facilitates the understanding of the difference in doping efficiency and σ. The electron donating building blocks (BDT, CPDT, and IDT) feature π-conjugation along the conjugated backbone direction, whereas the electron-withdrawing TTMN building block enables π-conjugation along the pendant direction. As shown in **Figure** 4a, because the strong electron-donating CPDT building block forms highly efficient π-conjugation along the conjugated backbone direction, $FeCl_3$ doping on the CPDT ring can make efficient charge delocalization along the backbone chain direction by stabilizing the quinoidal structure of the PTMN1, which is referred to as "backbone doping." The shallow HOMO energy level and high doping efficiency of PTMN1 are highly suitable for efficient backbone doping. In contrast, the weak electron-donating BDT moiety does not favor backbone doping because PTMN2 has a deep HOMO energy level and the lowest doping efficiency. However, it is expected that if the backbone doping is not preferred, TTMN pendant groups can act as a doping site by making a strong binding complex with $FeCl_4^-$ counter anion in the pendant side where large free volume exists. As shown in Figure 4b, if the $TTMN^+/FeCl_4^-$ binding complex are generated, the quinoidal structure of the TTMN pendant group is simultaneously developed, which enables efficient charge delocalization between the BDT and TTMN units. Consequently, pendant doping on the TTMN side can cause results similar to those of backbone doping. Importantly, pendant doping allows the dopants to make easier contact with the OTE polymer. Since conjugated backbones make strong intermolecular π-π stacking, direct backbone doping is not easy if the polymer does not have sufficient electron donating nature. Thus, PTMN2 with a deep HOMO energy level prefers pendant doping because $FeCl_3$ doping can occur in the lamellar ordering area where large free volume exists. Consequently, backbone doping on electron-sufficient PTMN1 boosted up the doping efficiency; however, it deteriorated σ at the high level of dopant concentration because $FeCl_4^-$ counter anions were working as impurities to interfere intermolecular ordering of PTMN1. In contrast, pendant doping of relatively electron-deficient PTMN2 exhibited a low doping efficiency; however, it interferes less with the intermolecular ordering of PTMN2 during the doping process because the process occurs outside the main backbone chain. In case of PTMN3, it

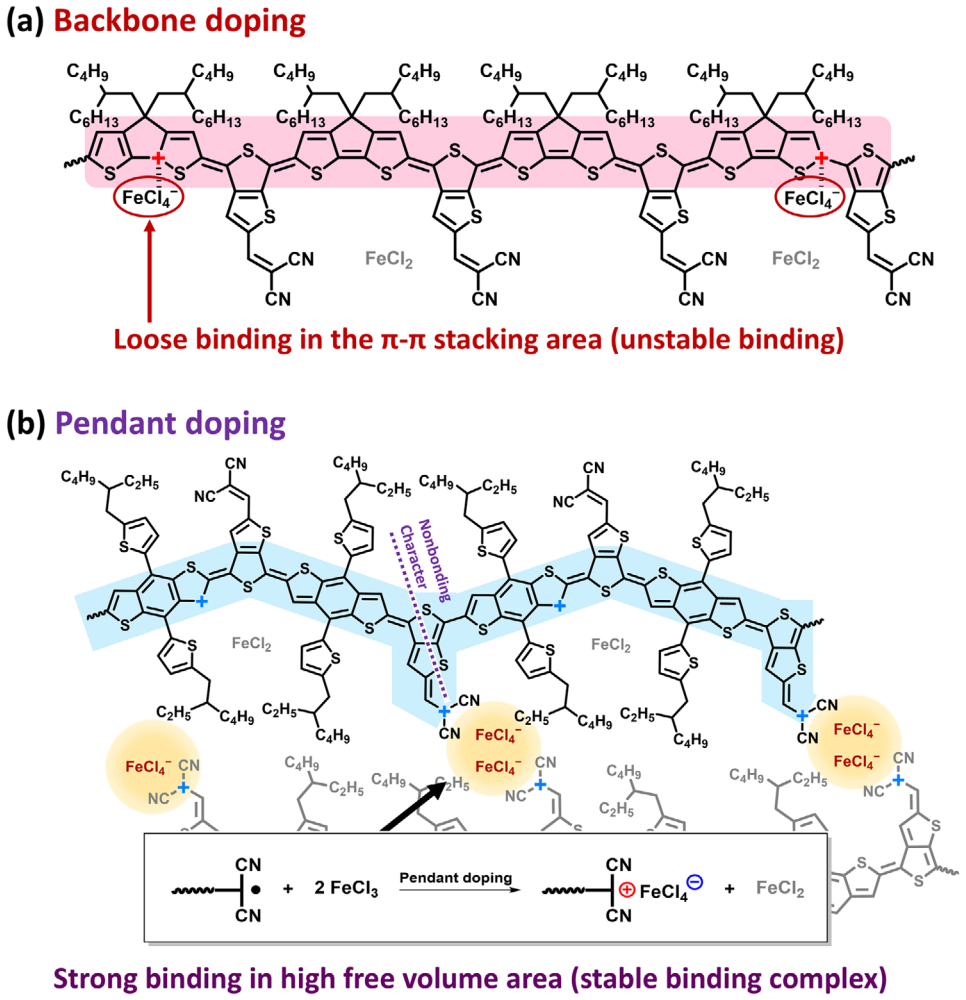

Figure 4. Suggested different doping mechanisms of a) PTMN1 and b) PTMN2 with $FeCl_3$ dopant.

showed different doping behavior with that of PTMN2. PTMN2 consistently showed linear I_{2500}/I_{ICT} ratio until 32 mM of $FeCl_3$, while PTMN3 showed steep increase of bipolaronic absorption higher than 6 mM of $FeCl_3$ (Figure 2). This strongly implies that PTMN3 initially prefers pendant doping like PTMN2, but as the dopant concentration increases, it gradually transitions to backbone doping, similar to PTMN1. Thus, the coexistence of backbone and pendant doping in PTMN3 appears to result in OTE properties that are intermediate between those of PTMN1 and PTMN2.

X-ray photoelectron spectroscopy (XPS) was performed to demonstrate the possibility of pendant doping. The strong electrostatic interaction between the bipolaronic cation of TTMN pendant and $FeCl_4^-$ counter anion affects the binding energy of the surrounding molecules. Particularly, because nitrogen is present only at the TTMN terminus in the polymer structure, the change in the nitrogen binding energy after doping signifies pendant doping with $FeCl_3$. As shown in **Figure** 5a, the N1s peaks of neat PTMN1, PTMN2, and PTMN3 films appeared at 399.5, 399.1, and 399.4 eV, respectively, with weak π–π^* satellite peaks, respectively, at 401.8, 401.4, and 401.9 eV, which refer to nitrogen of the TTMN building blocks. After $FeCl_3$ doping, the N1s peaks of the PTMN1, PTMN2, and PTMN3 films shifted to higher binding energies of 399.6, 399.5, and 399.9 eV, respectively. This implies that $FeCl_3$ doping reduced the electron density on the nitrogen atom by increasing its cationic characteristics. The degree of the N1s binding energy shifts for PTMN1, PTMN2, and PTMN3 were 0.1, 0.4, and 0.5 eV, respectively. The N1s binding energy of PTMN2 and PTMN3 significantly increased, which indicates pendant doping by forming strong interaction between the bipolaronic cation of TTMN pendant and $FeCl_4^-$ counter anion. In contrast, a small change in the N1s binding energy of PTMN1 indicates no preference for pendant doping.

Temperature-dependent σ was measured at temperatures in the range of 289 – 300 K, where the thermal de-doping process did not occur. Because the σ of the doped polymer films was proportional to temperature in this range, the Arrhenius correlation equation between the activation energy (E_a) and the σ can be expressed as Equation 1,

$$ln\ (\sigma) = ln\left(\sigma_\infty\right) - \frac{E_a}{k_B T} \quad (1)$$

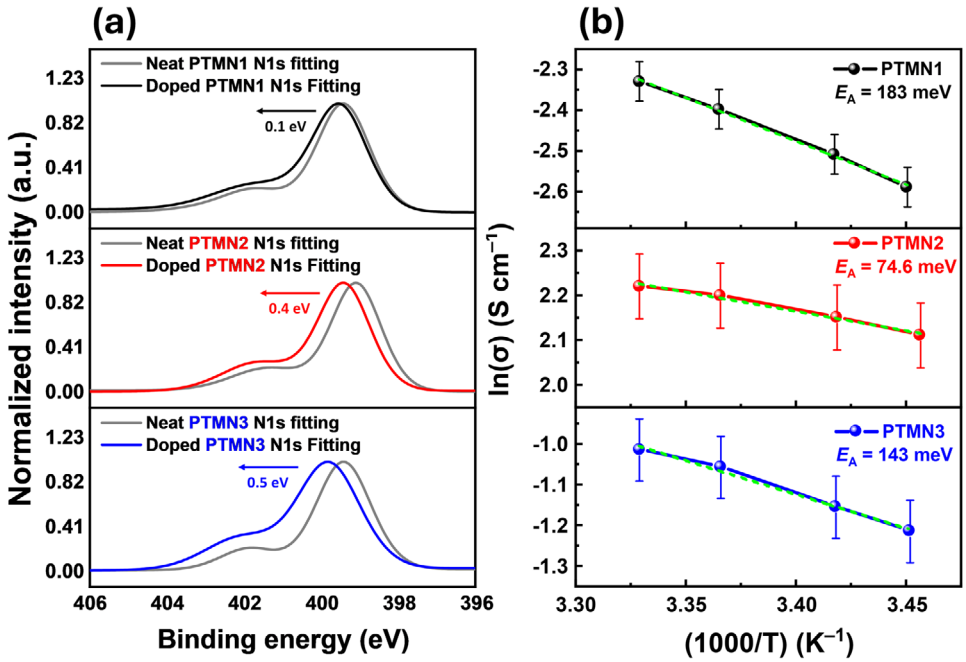

Figure 5. a) X-ray photoelectron spectroscopy (XPS) of N 1s peaks of PTMN1 (black line), PTMN2 (red line), and PTMN3 (blue line). b) The Arrhenius plot of electrical conductivity of OTE polymers. The $FeCl_3$ concentrations for the PTMN1, PTMN2, and PTMN3 samples are 4, 32, and 16 mM, respectively.

where σ_∞ is the temperature independent prefactor, E_a is the thermal activation energy, and k is the Boltzmann constant. As shown in Figure 5b and Figures S21 and S22 (Supporting Information), the fitted Arrhenius curve-derived E_a values were 183, 74.6, and 143 meV for PTMN1, PTMN2, and PTMN3, respectively. The E_a of PTMN2 was significantly lower than that of PTMN1 and PTMN3, indicating that hopping-type charge transport was facilitated in the doped PTMN2 film. This indicates that the doped PTMN2 film had the most efficient charge transport pathway, which can be attributed to pendant doping preventing dopant intercalation between the π-π stacking interfaces, thereby minimizing perturbation of the polymer morphology. In contrast, PTMN1 exhibited the highest E_a value, which indicates that hopping-type charge transport was not preferred owing to significant deterioration in the π-π stacking morphology of PTMN1 film by backbone doping.

The S of the OTE polymers was measured as a function of the $FeCl_3$ dopant concentration. It is well known that S has an inverse relationship with charge-carrier density in devices. Accordingly, the S values of the OTE polymers gradually decreased as the dopant concentration increased, as shown in Figure 3c. The S value of PTMN1 dropped sharply to close to zero in the early stage of $FeCl_3$ doping, whereas that of PTMN2 was much higher and maintained the high values, even at high dopant concentrations. The high doping efficiency and backbone doping of PTMN1 significantly increased the charge-carrier density, which significantly reduced S. As shown in Figure S23 (Supporting Information), backbone doping enhances π-conjugation along the polymer backbone direction, while forming some non-bonding interactions in the pendant direction. On the other hand, pendant doping of PTMN2 also increased the charge-carrier density on the conjugated backbone; however, it introduced partial non-bonding interactions in the conjugated backbones as quinoidal structures developed along the pendant direction, as shown in Figure 4b and Figure S23 (Supporting Information). It is presumed that the non-bonding interactions of the doped PTMN2 reduce the metallic characteristics and maintain high S values even at high dopant concentrations. The thermoelectric performances of PTMN1, 2, and 3 were evaluated by measuring the PF exhibited in Figure 3d.

Because only PTMN2 exhibited high σ and S, the PF of PTMN2 was the highest; that is, 12.8 μW m^{-1} K^{-2} at 16 mM $FeCl_3$ doping, which was 44 times higher than that of PTMN1 (0.29 μW m^{-1} K^{-2}) and 38 times higher than that of PTMN3 (0.34 μW m^{-1} K^{-2}) at the optimum doping condition. Notably, the high PF value of PTMN2 was not just a singular point value; rather, high PF values exceeding 10 μW m^{-1} K^{-2} were consistently maintained across a broad range of dopant concentrations (16–32 mM). The preferred pendant doping of PTMN2 appears to improve the OTE performance at high dopant concentrations by minimizing the morphological disorder of the polymers in the doped states.

Doping stability was measured by the changes in TE properties of $FeCl_3$-doped PTMN1–3 films over time under N_2 conditions (Figure S24, Supporting Information). $FeCl_3$-doped PTMN1 and PTMN3 films exhibited negligible changes in σ, S, and PF, while PTMN2 showed a decrease in σ but an increase in S over time, resulting in a constant PF that maintained over 90% of its initial value after three days (PTMN1: 6.1% increase, PTMN3: 18.5% decrease). Considering that PTMN2 contains 2 times and 8 times higher dopant concentration than PTMN3 and PTMN1, respectively, the maintenance of a high PF suggests that the pendant doping contributes to the stabilization of the excessive dopant residues in the devices. Additionally, the doping stability of

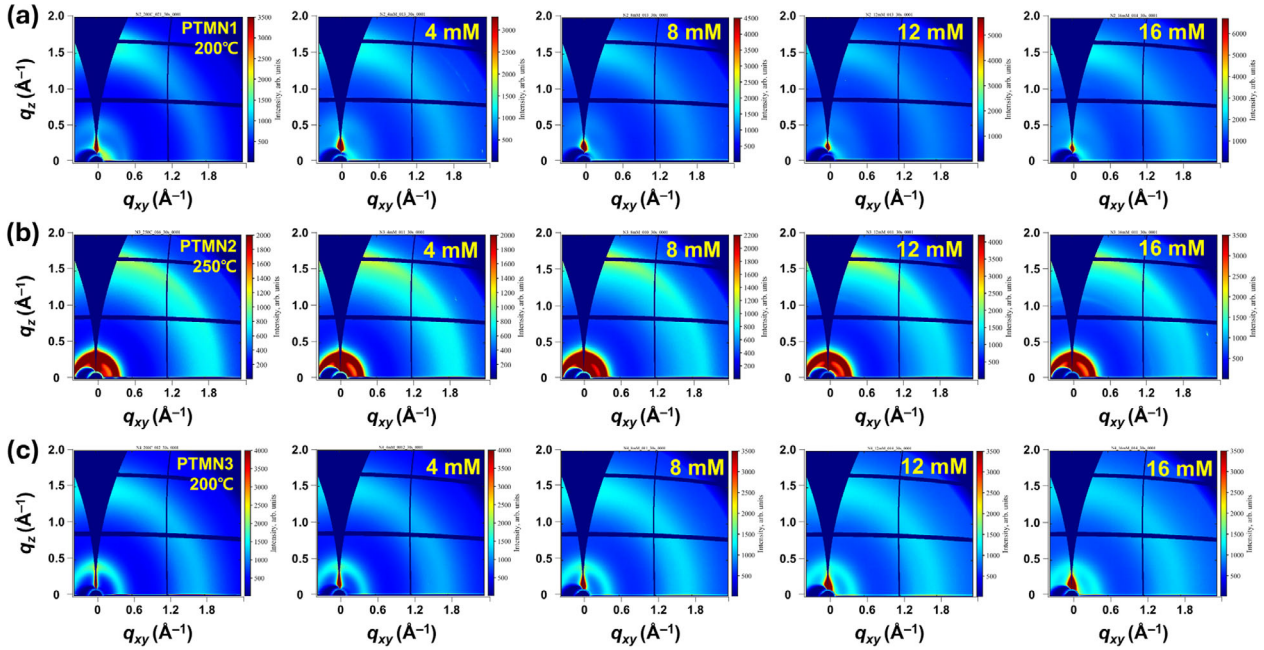

Figure 6. 2D-GIXD pattern images of PTMN1–3 with various $FeCl_3$ concentrations. a) PTMN1 (200 °C, 4–16 mM), b) PTMN2 (250 °C, 4–16 mM), and c) PTMN3 (200 °C, 4–16 mM) with color bars.

$FeCl_3$-doped poly(3-hexylthiophene-2,5-diyl) (P3HT), a representative conjugated polymer in OTE devices, was compared to that of PTMN1–3 films. $FeCl_3$-doped P3HT films also showed a reduction in σ, but a slight increase in the S of P3HT films, resulting in a 38.5% decrease in PF after three days. Therefore, the pendant doping of PTMN2 could contribute to maintaining a high PF in OTE devices by promoting high S values.

2.4. Morphological Properties

To investigate the morphological properties of the synthesized OTE polymers, 2D grazing incident X-ray diffraction (2D-GIXD) patterns were obtained as functions of the annealing temperature (Figure S25a–c, Supporting Information) with the line-cut profiles along the q_z and q_{xy} axes (Figure S26a–f, Supporting Information). (100) lamellar ordering peaks of PTMN1 and PTMN3 were not very clear along the q_z and q_{xy} axes; however, that of PTMN2 appeared sharply at 0.28 Å^{-1} along the q_{xy} axis, corresponding to the d-spacing distance of 22.3 Å. Only PTMN2 exhibited excellent lamellar stacking ordering in the pristine films. In the case of (010) π–π stacking ordering area (1.4–1.8 Å^{-1}), the PTMN1 and PTMN3 pristine films showed dominant broad diffraction peak at 1.5 Å^{-1}, whereas PTMN2 exhibited dual diffraction peak at 1.4 and 1.7 Å^{-1} of similar intensities along the q_z axis. Only PTMN2 showed a clear (010) diffraction peak at ≈1.7 Å^{-1}, which corresponds to the d-spacing of 3.6 Å. Morphological changes in the pristine films were observed by thermal annealing, as shown in Figure S25a–c (Supporting Information). The π–π stacking ordering of PTMN1 was gradually enhanced at annealing temperatures up to 200 °C; however, it drastically decreased above this temperature. In the case of PTMN2, (100) peak along the q_{xy} axis and (010) peaks along the q_z axis became clearer and stronger even at 250 °C, which indicates enhanced face-on orientation during the annealing process. Meanwhile, PTMN3 did not show any strong diffraction peaks during thermal annealing, indicating its dominantly amorphous nature. To visualize the changes in the (010) π–π stacking ordering peak with respect to the annealing temperature, the azimuthal cut of the (010) peak along q_z as a function of the annealing temperature was extracted as shown in Figure S27a–c (Supporting Information). The (010) peaks of pristine PTMN1 and PTMN3 films were diminished at high annealing temperature, whereas those of pristine PTMN2 film gradually increased and maximized at 250 °C. Consequently, PTMN2 exhibited better molecular ordering and orientation in the face-on mode.

To investigate the morphological changes in the OTE polymers during $FeCl_3$ doping, the 2D-GIXD diffraction pattern of the doped OTE polymer films was determined as a function of the dopant concentration (**Figure 6**a–c) with line-cut profiles along the q_{xy} and q_z axes (**Figure 7**a–f). As shown in Figure 6a, the broad (010) π-π stacking peak of PTMN1 film gradually disappeared as the dopant concentration increased, indicating that its molecular ordering has been deteriorated by $FeCl_3$. Furthermore, the d-spacing of the (010) peak of PTMN1 at 1.7 Å^{-1} increased from 4.2 to 4.4 Å along the q_{xy} axis and from 3.5 to 3.7 Å along the q_z axis depending on the dopant concentration, which strongly indicates that $FeCl_3$ dopant weakens the π–π stacking of PTMN1. In contrast, the (010) π–π stacking peak of PTMN2 films remained strong even at high dopant concentration (Figure 6b), indicating that $FeCl_3$ dopant does not have a significant impact on the π–π stacking of PTMN2. As expected, the backbone doping on PTMN1 weakened the π-π stacking ordering, whereas the pendant doping on PTMN2 gave little impact on the π–π stacking ordering even at high dopant concentration. PTMN3 exhibited the weakest diffraction pattern; its molecular ordering weakened

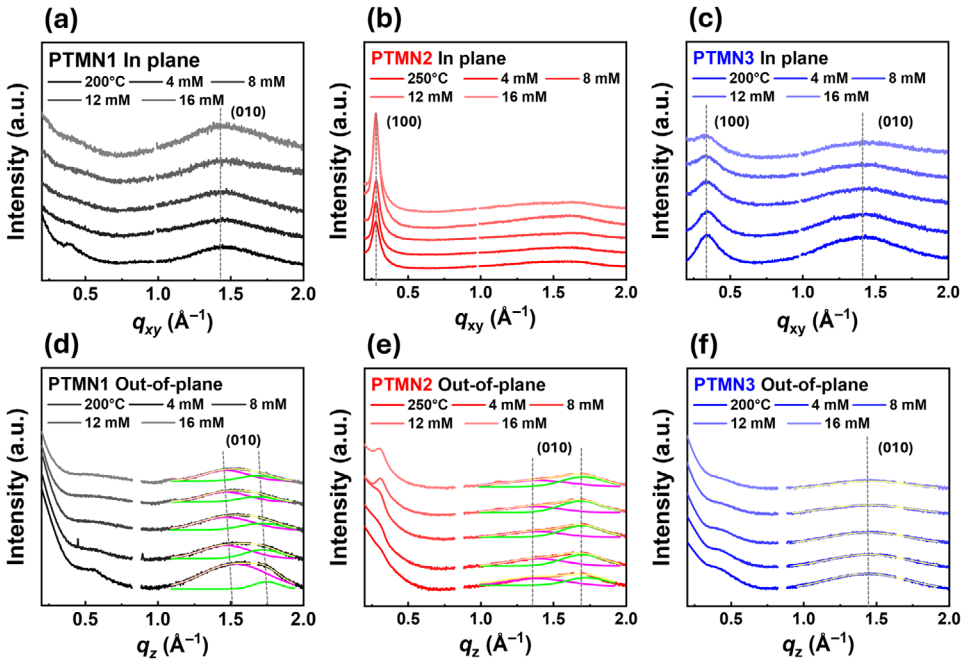

Figure 7. The line-cut profiles of doped OTE polymers with different dopant concentration along the a–c) q_{xy} axis, and d–f) q_z axis; PTMN1 (black line), PTMN2 (red line), PTMN3 (blue line). The magenta and green lines indicate deconvoluted (010) peak of OTE polymers.

as the dopant concentration increased and the *d*-spacing distance increased.

Additionally, the q_z line-cut profiles relative to the background intensity (0.75–1.0 Å^{-1}) were normalized to compare the change in the 2D-GIXD peak intensities as a function of dopant concentration. As shown in Figure S28 (Supporting Information), PTMN2 exhibited minimal changes in the intensity of the (010) peak with increasing $FeCl_3$ concentration. In contrast, PTMN1 showed a significant change in the (010) peak intensity, as well as a notable decrease in peak intensity of 0.5 Å^{-1} after doping, clearly indicating the disruption of molecular ordering. Similarly, PTMN3 also showed a decrease in peak intensity ≈0.3–0.5 Å^{-1}.

Consequently, a significant decrease in σ and PF of PTMN1 was caused by the disrupted intermolecular ordering owing to $FeCl_3$ doping, whereas the high electrical conductivity and PF of PTMN2 under heavy doping were attributed to the retained excellent face-on ordering during the doping process. In detail, the preferred pendant doping in PTMN2 promotes efficient Coulombic interactions between the positively charged malononitrile group in the pendant side and the $FeCl_4^-$ anion (Figure 4b), preventing morphological deterioration of the polymer films and resulting in higher OTE performance even at high dopant concentrations (≈32 mM). PTMN3, containing bulky IDT backbone, exhibited amorphous ordering characteristics, which resulted in lower σ and PF values than those of PTMN2.

2.5. Thermal Conductivity and ZT Values

Thermal conductivities (κ) of doped PTMN1–3 films at 300 K were measured via 3-omega method with dual membrane correction to increase the measurement accuracy. The $FeCl_3$-doped PTMN1 (4 mM), PTMN2 (32 mM), PTMN3 (16 mM) films exhibited κ values of 0.189, 0.212, and 0.262 W m^{-1} K^{-1}, respectively, which are in the range of the κ values for amorphous conjugated polymers (0.15–0.4 W m^{-1} K^{-1}).[31] Notably, the PTMN2 film with a high dopant concentration still exhibited low κ values, comparable to those of PTMN1 films with a low dopant concentration. In the case of PTMN3, it exhibited higher κ values (0.26–0.30 W m^{-1} K^{-1}) than those of the other polymers, but the values decreased at higher dopant concentrations. To understand the different κ behaviors, the relationship between polymer structure and κ values was analyzed. In general, κ is given by the sum of the lattice contribution (κ_L) and the electronic contribution (κ_e) ($\kappa = \kappa_L + \kappa_e$). According to the Wiedemann-Franz law ($\kappa_e = L\sigma T$, where L is the Lorenz factor of 2.45×10^{-8} V^2 K^{-2}), the κ_e can be evaluated from the measured σ.[57,58] The calculated upper limit of κ_e values was as low as 0.0001, 0.0043, and 0.0001 for doped PTMN1, PTMN2, and PTMN3, respectively. Thus, κ_L is the dominant factor determining the κ values, which strongly depend on the microstructure of the conjugated polymer films.

Rodríguez-Martínez et al. suggested that the κ_L values decreased with increasing free volume fraction within the polymer films, thereby interfering heat dissipation.[31] Thus, the free volume fraction of the PTMN1–3 films was compared using the molar mass of the side chains (Da) and unit cell volume (Å^3) of the PTMN1–3 polymers (unit cell volumes were estimated from the crystallographic parameters in Tables S3–S8, Supporting Information). As shown in Table S9 (Supporting Information), calculated molar mass of side chain per unit cell of the polymer was clearly higher for PTMN3 (0.517 Da/Å^3) compared to PTMN1 (0.345 Da/Å^3) and PTMN2 (0.394 Da/Å^3), indicating that PTMN3 film have the lowest free volume fraction among the polymers. This result implied that the higher κ values on doped PTMN3

Table 2. Summary of thermoelectric properties.

Material	$FeCl_3$ concentration [mM]	Σ [S cm^{-1}]	S [μV K^{-1}]	PF [μW m^{-1} K^{-2}]	K [W m^{-1} K^{-1}]	ZT
PTMN1[a)]	2	0.103 (±0.016)	168 (±2.0)	0.19 (±0.02)	–	–
	4	0.147 (±0.014)	40.5 (±2.2)	0.02 (±0.002)	0.189 (±0.02)	3.17×10^{-5} ($\pm 3 \times 10^{-6}$)
PTMN2[b)]	16	1.792 (±0.284)	268 (±1.2)	12.8 (±2.04)	0.190 (±0.02)	0.020 (±0.003)
	32	5.885 (±1.110)	131 (±1.4)	10.1 (±1.90)	0.212 (±0.02)	0.014 (±0.003)
PTMN3[a)]	4	0.019 (±0.004)	42.4 (±1.2)	0.34 (±0.07)	0.298 (±0.03)	3.42×10^{-4} ($\pm 7.0 \times 10^{-5}$)
	16	0.152 (±0.020)	2.2 (±2.5)	0.01 (±0.001)	0.262 (±0.03)	1.15×10^{-4} ($\pm 1.3 \times 10^{-6}$)

Annealed at [a)] 200 °C and [b)] 250 °C.

films than those of doped PTMN1 and PTMN2 films are due to the higher density of side chains, which assist the propagation of heat through the polymer films. Finally, the ZT values were calculated from the PF and κ values, which was 3.17×10^{-5} for PTMN1 (4 mM), 0.020 for PTMN2 (16 mM) and 3.42×10^{-4} for PTMN3 (4 mM), respectively. The molecular structure of PTMN2 not only enhances the S through pendant doping, but also facilitates a reduction in κ, making it a promising material for TE applications. The TE performance is summarized in **Table 2** and Figure S2 (Supporting Information).

Furthermore, since the lattice contribution to κ was highly dominant while the electronic contribution was very small (< 0.001 W m^{-1} K^{-1}), it is expected that the changes in κ values of PTMN2 and PTMN3 with increasing $FeCl_3$ concentration were not due to changes in σ, but rather the result of changes in the microstructure of the films caused by $FeCl_3$ doping. As confirmed by 2D-GIXD analysis (Figure 6; Figure S28, Supporting Information), the molecular ordering of PTMN1 and PTMN3 was significantly disrupted by $FeCl_3$ doping. Thus, the disorder-induced phonon scattering hindered heat transport,[59] leading to the decrease of κ values of PTMN3 from 0.298 W m^{-1} K^{-1} (4 mM) to 0.262 W m^{-1} K^{-1} (16 mM). Contrarily, $FeCl_3$-doped PTMN2 maintained its molecular ordering well through the pendant doping mechanism, preventing disorder-induced phonon scattering, which might have led to an increase in κ values from 0.190 W m^{-1} K^{-1} (16 mM) to 0.212 W m^{-1} K^{-1} (32 mM). Although the pendant doping mechanism of PTMN2 slightly increased κ values by maintaining molecular ordering, we believe that it contributes to improved ZT due to its more significant impact on enhancing σ.

3. Conclusion

An electron-withdrawing TTMN monomer was synthesized and copolymerized with three different electron-donating conjugated building blocks (CPDT, BDT, and IDT) through the Stille coupling reaction, which resulted in novel TTMN-based conjugated polymers named PTMN1, PTMN2, and PTMN3. All the synthesized OTE polymers possessed extended π-conjugation along the pendant side owing to the unique molecular structure of the TTMN moiety. Interestingly, PTMN1 and PTMN2 exhibited completely different doping characteristics depending on the dopant concentration. PTMN1 exhibited excellent doping efficiency with strong bipolaron absorption after $FeCl_3$ doping, whereas PTMN2 demonstrated the lowest doping efficiency with the coexistence of neutral and bipolaron absorption, even under heavy doping. Furthermore, from the XPS study, it was found that the TTMN moiety on PTMN2 had strong binding with $FeCl_4^-$ counter anions, indicating pendant doping, whereas PTMN1 did not show any evidence for pendant doping. Therefore, it is suggested that PTMN1 having shallow HOMO energy levels and electron-sufficient backbone chains prefer backbone doping with excellent doping efficiency, whereas PTMN2 having deep HOMO energy levels and less electron-sufficient backbone chains do not prefer efficient backbone doping (low doping efficiency), however, they rather prefer pendant doping by forming strong binding complex between TTMN and $FeCl_4^-$. Notably, the intermolecular ordering of PTMN1 was significantly decreased by backbone doping with $FeCl_3$, which resulted in low σ and PF at high dopant concentrations. However, the intermolecular ordering of PTMN2 was well preserved even under high-concentration doping, which is attributed to pendant doping with $FeCl_3$ and resulted in the highest σ and S. Consequently, the PF of PTMN2 reached 12.8 μW m^{-1} K^{-2}, which was 44 times higher than that of PTMN1 (0.29 μW m^{-1} K^{-2}). Interestingly, the high PF value of PTMN2 was not just a singular point value; rather, high PF values exceeding 10 μW m^{-1} K^{-2} were consistently maintained across a broad range of high dopant concentrations (16–32 mM). The favored pendant doping in PTMN2 enhanced the OTE performance at high dopant concentrations by retaining $FeCl_4^-$ counter anion at the terminal end of the TTMN moiety, which minimized the morphological disorder in the doped polymers. This unique doping behavior on the pendant side opens up new possibilities for the development of high-performance OTE polymers.

4. Experimental Section

Measurement: The absorption spectra of the thermoelectric polymers were measured using a JASCO V-730 UV–vis spectrometer. The UV–vis–NIR absorption spectra of the doped thermoelectric polymers were

recorded using a JASCO V-670 spectrometer. The ^{1}H nuclear magnetic resonance (NMR) spectra of the thieno[3,4-*b*]thiophene derivative monomers and thermoelectric polymers were recorded at 25 °C using a VNMRS spectrometer and a Bruker Ascend TM-400 spectrometer for 600 and 400 MHz, respectively. Cyclic voltammetry measurements were performed at a scan rate of 20 mV s^{-1} using a WonATech potentiostat/galvanostat/impedance analyzer ZIVE SP1(1A), with a three-electrode cell and a 0.1 M Bu_4NPF_6 solution in acetonitrile as the electrolyte. The working electrode was coated with the polymer films by dipping them into their solutions in chloroform. The molecular weight measurement of thermoelectric polymers was recorded by Agilent 1260 Infinity II GPC at 35 °C. The thermal stability measurement was performed by thermogravimetric analysis using TA instruments Discovery TGA550 Auto, under nitrogen flow with a heat rate of 10 °C mins^{-1} and a temperature range from 30 to 500 °C. 2D grazing incident X-ray diffraction (2D-GIXD) measurements were performed using a high-resolution synchrotron X-ray beam source (beam energy = 9.3 keV) with a grazing incidence angle of ≈0.16° at the 3C beamline of the Pohang Accelerator Laboratory (PAL) in Pohang, Korea. The *d*-spacing values were calculated using the following relation: $q = 2\pi/d$, where q denotes the specific diffraction peak position. The sheet resistances (RS) of $FeCl_3$ doped OTE polymers were measured using a 4-point probe (where each tip was separated by 1 mm) connected to a Keithley 2400 source meter in an N_2-filled glove box. The film thicknesses were measured using a surface profiler (Alpha Step IQ, KLA Tencor). Then, σ was calculated using the measured RS and thickness values. The *S* value was measured in a N_2-filled glove box using the same in-house setup developed and used in the previous studies.[60–63] The OTE polymer-based samples were placed between two Peltier devices (separated by 1 cm), each of which was operated using a Keithley 2400 source meter to induce a temperature gradient. Thermovoltages were measured using a Keithley 4200-SCS parameter analyzer, and temperatures were measured using a Keithley 2700 multimeter.

OTE Device Fabrication: Soda-lime glass substrates (2 × 2 cm) were cleaned using bath sonication in deionized water with detergent, followed by successive sonication in acetone and ethanol for 20 min each. Titanium/gold (4 nm/40 nm) electrodes were deposited on top of the cleaned substrates by thermal evaporation through a shadow mask (inter-electrode distance: 8 mm) to measure the *S* value. The OTE polymers and $FeCl_3$ were dissolved in chloroform and acetonitrile with a concentration of 10 mg mL^{-1} and 1–32 mM, respectively. The polymer solutions were spin-coated at 1000 rpm for 45 s on UV/ozone-treated glass substrates and then annealed at various temperatures for 15 min on a hotplate. Thereafter, $FeCl_3$ solutions were poured onto the annealed films during spin coating at 4000 rpm for 20 s.

Materials: All anhydrous solvents were purchased from Sigma–Aldrich. Tetrakis(triphenylphosphine)palladium(0) was purchased from Sejin-CI (South Korea). 3,4-dibromothiophene, (4,8-bis(5-(2-ethylhexyl)thiophen-2-yl)benzo[1,2-*b*:4,5-*b*′]dithiophene-2,6-diyl)bis(trimethylstannane) and (4,4,9,9-tetrakis(4-hexylphenyl)-4,9-dihydro-*s*-indaceno[1,2-*b*:5,6-*b*′]dithiophene-2,7-diyl)bis(trimethylstannane) were provided by J's science (South Korea). All chemicals were used without further purification. Compounds 1–4 were synthesized according to previously reported procedures.[64] TTMN and compound 5 were synthesized using a procedure similar to that reported in the literature.[51]

Synthesis of thieno[3,4-b]thiophene Derivative Monomers: 4-bromothiophene-3-carbaldehyde (1): 3,4-dibromothiophene (10 g, 41.33 mmol) was dissolved in dry diethyl ether (100 mL) and stirred at room temperature for 10 min. As the reaction mixture was cooled down to −78 °C with a dry ice dewar, n-butyl lithium (2.5 M, 16.5 mL) was slowly added dropwise. After 30 min, dimethylformamide (3.32 g, 41.33 mmol) was added, and the mixture was stirred for 2 h. The crude mixture was then poured into water: diethyl ether (1:1) solution. The combined organic layers were extracted three times with diethyl ether and washed with water and brine. The organic layer was then dried using $MgSO_4$ and filtered. The solvent was removed using a rotary evaporator to obtain compound 1 as a brownish liquid (6.48 g, 82.1%) without further purification. ^{1}H NMR (600 MHz, $CDCl_3$), δ (ppm): 9.90 (s, 1H), 8.12 (d, 1H, J = 3.6 Hz), 7.33 (d, 1H, J = 3.6 Hz).

Ethyl thieno[3,4-b]thiophene-2-carboxylate (2): Potassium carbonate (10.9 g, 78.6 mmol) and copper oxide nano-powder (62.8 mg, 0.79 mmol) were suspended in dry dimethyl formamide (50 mL) and refluxed at 60 °C. As the reaction temperature was attained, ethyl thioglycolate (3.15 g, 26.2 mmol) and 4-bromothiophene-3-carbaldehyde (compound 1; 5 g, 26.2 mmol) were added and refluxed overnight. The crude mixture was filtered to remove residual inorganic salts, and the filtrate was poured into a water: ethyl acetate (1:1) solution. The combined organic layers were extracted three times with ethyl acetate and washed with water and brine. Thereafter, the organic layer was dried using $MgSO_4$, and the solvent was removed using a rotary evaporator. The crude product was purified by column chromatography using ethyl acetate: hexane (1:10) as the eluent. Compound 2 was obtained as an off-white powder (2.32 g, 41.7%) by recrystallization from methylene chloride: hexane at −20 °C. ^{1}H NMR (400 MHz, $CDCl_3$), δ (ppm): 7.70 (sd, 1H, J = 0.8 Hz), 7.59 (d, 1H, J = 2.4 Hz), 7.29 (dd, 1H, J = 2.8 Hz, 0.8 Hz), 4.39 (q, 2H, J = 7.2 Hz), 1.40 (t, 3H, J = 7.2 Hz). ^{13}C NMR (100 MHz, $CDCl_3$), δ (ppm): 163.29, 146.06, 139.92, 123.61, 116.74, 111.50, 61.78, 14.44.

Thieno[3,4-b]thiophen-2-ylmethanol (3): Ethylthieno [3,4-*b*]thiophene-2-carboxylate (compound 2; 2 g, 9.42 mmol) was dissolved in dry diethyl ether (30 mL) and stirred at room temperature. Lithium aluminum hydride (4 M in diethyl ether, 2.36 mL) was slowly added to the reaction mixture and stirred for 2 h. The crude mixture was poured into chloroform (150 mL) and stirred. The 1.0 M sodium hydroxide solution (100 mL) was added dropwise to the crude mixture using a glass pipette. (Caution: A large amount of gas and heat was released during this step.) The crude mixture was stirred for 1 h to remove any reactive species before extracting the combined organic layer three times with ethyl acetate. The extracted organic layers were washed with water and brine and dried using $MgSO_4$, and the solvent was removed using a rotary evaporator. Thereafter, the crude product was purified through column chromatography using hexane: ethyl acetate (1:8) as the eluent. Compound 3 was obtained as a white powder (920.5 mg, 57.4%) by recrystallization from methylene chloride: hexane at −20 °C. ^{1}H NMR (600 MHz, $CDCl_3$), δ (ppm): 7.27 (sd, 1H, J = 2.4 Hz), 7.21 (sd, 1H, J = 2.4 Hz), 6.84 (s, 1H), 4.78 (s, 2H), 1.89 (br, 1H). ^{13}C NMR (100 MHz, $CDCl_3$), δ (ppm): 150.88, 146.87, 138.90, 114.48, 112.20, 111.04, 61.71.

Thieno[3,4-b]thiophene-2-carbaldehyde (4): Thieno[3,4-*b*]thiophen-2-ylmethanol (compound 3; 1 g, 5.87 mmol) was dissolved in methylene chloride (15 mL), and the mixture was stirred. Pyridinium chlorochromate (PCC; 1.27 g, 5.87 mmol) was added in several portions. The reaction mixture was stirred overnight, and the residual PCC and inorganic salts were filtered out. The brownish filtrate was poured into water:methylene chloride (1:1) solution and the combined organic layer was extracted three times with methylene chloride and washed several times with water and brine. The organic layer was then dried using $MgSO_4$. The solvent was removed using a rotary evaporator to obtain compound 4 as a brownish, dense liquid, which was immediately used for the next step. ^{1}H NMR (600 MHz, $CDCl_3$), δ (ppm): 10.0 (s, 1H), 7.76 (d, 1H, J = 2.4 Hz), 7.68 (s, 1H), 7.33 (d, 1H, J = 3.0 Hz).

2-(thieno[3,4-b]thiophen-2-ylmethylene)malononitrile (TTMN): Thieno[3,4-*b*]thiophene-2-carbaldehyde (compound 4; 1 g, 5.94 mmol), malononitrile (431.64 mg, 6.53 mmol), and an excess amount of aluminum oxide (activated, neutral, Brockmann) were suspended in methylene chloride (30 mL) and stirred overnight at room temperature. After the reaction was complete, the reaction mixture was filtered to remove residual aluminum oxide. The reaction mixture was then poured into a water: methylene chloride (1:1) solution. The combined organic layers were extracted three times with methylene chloride and washed several times with water and brine. Thereafter, the organic layer was dried using $MgSO_4$, and the solvent was removed using a rotary evaporator. TTMN was obtained as a yellow solid (993.1 mg, 77.3%) by recrystallization from methylene chloride: hexane. ^{1}H NMR (600 MHz, $CDCl_3$), δ (ppm): 7.83 (s, 1H), 7.79 (d, 1H, J = 3.6 Hz), 7.60 (s, 1H), 7.37 (d, 1H, J = 2.4 Hz). ^{13}C NMR (100 MHz, DMSO-d6), δ (ppm): 155.16, 144.47, 140.89, 138.89, 132.60, 122.11, 114.33, 113.70, 113.29, 112.14, 78.43.

2-((4,6-dibromothieno[3,4-b]thiophen-2-yl)methylene)malononitrile (5): TTMN (1 g, 4.62 mmol) and *N*-bromosuccinimide (904.19 mg,

5.08 mmol) were dissolved in dimethyl formamide (30 mL) and stirred at 0 °C overnight. The progress of the reaction was monitored through thin-layer chromatography. Once the reaction was complete, the mixture was poured into a water: methylene chloride (1:1) solution. The combined organic layers were extracted three times with methylene chloride and washed several times with water and brine. Thereafter, the organic layer was dried using $MgSO_4$, and the solvent was removed using a rotary evaporator. The crude product was purified through column chromatography using methylene chloride: hexane (1:1) as the eluent. Compound 5 was obtained as an orange solid (1.51 g, 87.2%) by recrystallization from methylene chloride: hexane. ^{1}H NMR (600 MHz, $CDCl_3$), δ (ppm): 7.78 (s, 1H), 7.41 (s, 1H).

General Procedure for Polymerization: Compound 5 (1 equiv), the respective stannyl compound (1 equiv), and tetrakis(triphenylphosphine)palladium(0) (0.03 eq) were added to a 10 mL reaction vial for microwave irradiation. The reaction vial was evacuated and refilled with N_2 gas three times, and dry toluene/DMF (5 mL, 7:3 ratio) was added. The reaction was performed in a Biotage microwave reactor at 170 °C for 2 h. After the polymerization, the crude polymer was filtered through a Celite 545 filter and precipitated in methanol. The collected polymers were extracted by using a Soxhlet extractor containing methanol, acetone, and chloroform. Chloroform was concentrated and subsequently precipitated in methanol. The final thermoelectric polymer was collected by filtration and dried under vacuum.

Poly[(4,4-bis(2-butyloctyl)-4H-cyclopenta[2,1-b:3,4-b′]dithiophene-2,6-diyl)-alt-(2-(thieno[3,4-b]thiophen-2-ylmethylene)malononitrile-4,6-diyl)] (PTMN1)

(4,4-Bis(2-butyloctyl)-4*H*-cyclopenta[2,1-*b*:3,4-*b*']dithiophene-2,6-diyl)bis(trimethylstannane) (252.16 mg, 0.3 mmol), and compound 5 (112.22 mg, 0.3 mmol) were used for the polymerization of PTMN1 as stannyl- and bromo-compounds, respectively. The final polymer was obtained as a dark solid (116.93 mg, 53.6%).

Poly[(4,8-bis(5-(2-ethylhexyl)thiophen-2-yl)benzo[1,2-b:4,5-b′]dithiophene-2,6-diyl)-alt-2-(thieno[3,4-b]thiophen-2-ylmethylene)malononitrile-4,6-diyl] (PTMN2)

(4,8-Bis(5-(2-ethylhexyl)thiophen-2-yl)benzo[1,2-*b*:4,5-*b*']dithiophene-2,6-diyl)bis(trimethylstannane) (271.37 mg, 0.3 mmol), and compound 5 (112.22 mg, 0.3 mmol) were used for the polymerization of PTMN2 as stannyl- and bromo-compounds, respectively. The final polymer was obtained as a dark solid (159.27 mg, 67.1%).

Poly[(4,4,9,9-tetrakis(4-hexylphenyl)-4,9-dihydro-s-indaceno[1,2-b:5,6-b′]dithiophene-2,7-diyl)-alt-2-(thieno[3,4-b]thiophen-2-ylmethylene)malononitrile-4,6-diyl] (PTMN3)

(4,4,9,9-Tetrakis(4-hexylphenyl)-4,9-dihydro-*s*-indaceno[1,2-*b*:5,6-*b*']dithiophene-2,7-diyl)bis(trimethylstannane) (369.91 mg, 0.3 mmol), and compound 5 (112.22 mg, 0.3 mmol) were used for the polymerization of PTMN3 as stannyl- and bromo-compounds, respectively. The final polymer was obtained as a dark solid (228.92 mg, 59.5%).

Supporting Information

Supporting Information is available from the Wiley Online Library or from the author.

Acknowledgements

H.K. and S.B.K. contributed equally to this work. This research was supported by the Nano & Material Technology Development Program of the National Research Foundation of Korea (NRF), funded by the Ministry of Science and ICT (RS-2024-00402972 and RS-2023-00281944), and also supported by the NRF grant funded by the Korea government (MSIT) (RS-2024-00398065).

Conflict of Interest

The authors declare no conflict of interest.

Data Availability Statement

The data that support the findings of this study are available in the supplementary material of this article.

Keywords

conjugated polymers, organic thermoelectrics, pendant doping, side-chain conjugation, side-chain interaction

Received: November 21, 2024
Revised: January 4, 2025
Published online: January 23, 2025

[1] J. H. Lee, K. H. Cho, K. Cho, *Adv. Mater.* **2023**, *35*, 2209673.
[2] M. Sang, K. Kang, Y. Zhang, H. Zhang, K. Kim, M. Cho, J. Shin, J. H. Hong, T. Kim, S. K. Lee, *Adv. Mater.* **2022**, *34*, 2105865.
[3] Y. E. Shin, Y. J. Park, S. K. Ghosh, Y. Lee, J. Park, H. Ko, *Adv. Sci.* **2022**, *9*, 2105423.
[4] Z. Chu, W. Jiao, Y. Huang, Y. Zheng, R. Wang, X. He, *J. Mater. Chem. A* **2021**, *9*, 9634.
[5] X. He, Y. Hao, M. He, X. Qin, L. Wang, J. Yu, *ACS Appl. Mater. Interfaces* **2021**, *13*, 60498.
[6] G. Liu, Z. Lv, S. Batool, M. Z. Li, P. Zhao, L. Guo, Y. Wang, Y. Zhou, S. T. Han, *Small* **2023**, *19*, 2207879.
[7] H. Liu, D. Liu, J. Yang, H. Gao, Y. Wu, *Small* **2023**, *19*, 2206938.
[8] Q. Ye, Z. Chen, D. Yang, W. Song, J. Zhu, S. Yang, J. Ge, F. Chen, Z. Ge, *Adv. Mater.* **2023**, *35*, 2305562.
[9] S. Duan, Q. Shi, J. Hong, D. Zhu, Y. Lin, Y. Li, W. Lei, C. Lee, J. Wu, *ACS Nano* **2023**, *17*, 1355.
[10] S. Lee, J. Kim, H. Roh, W. Kim, S. Chung, W. Moon, K. Cho, *Adv. Mater.* **2022**, *34*, 2109545.
[11] X. Yue, F. Xu, L. Zhang, G. Ren, H. Sheng, J. Wang, K. Wang, L. Yu, J. Wang, G. Li, *ACS Sens.* **2022**, *7*, 2198.
[12] D. S. Anisimov, A. A. Abramov, V. P. Gaidarzhi, D. S. Kaplun, E. V. Agina, S. A. Ponomarenko, *ACS Omega* **2023**, *8*, 4649.
[13] W. Wei, S. Zhou, D. D. Ma, Q. Li, M. Ran, X. Li, X. T. Wu, Q. L. Zhu, *Adv. Funct. Mater.* **2023**, *33*, 2302917.
[14] X. Yan, D. Su, H. Li, X. Zhao, X. Liu, F. Liu, P. Sun, G. Lu, *Adv. Funct. Mater.* **2023**, *33*, 2215192.
[15] J. H. Lee, S. P. Park, K. Park, H. J. Kim, *Adv. Funct. Mater.* **2020**, *30*, 1907437.
[16] H. Park, S. Kim, J. Lee, I. Lee, S. Bontapalle, Y. Na, K. Sim, *Nat. Electron.* **2024**, *7*, 39.
[17] L. Sun, J. Wang, H. Matsui, S. Lee, W. Wang, S. Guo, H. Chen, K. Fang, Y. Ito, D. Inoue, *Sci. Adv.* **2024**, *10*, eadk9460.
[18] G. H. Kim, L. Shao, K. Zhang, K. P. Pipe, *Nat. Mater.* **2013**, *12*, 719.
[19] Q. Zhang, Y. Sun, W. Xu, D. Zhu, *Adv. Mater.* **2014**, *26*, 6829.
[20] B. Russ, A. Glaudell, J. J. Urban, M. L. Chabinyc, R. A. Segalman, *Nat. Rev. Mater.* **2016**, *1*, 16050.
[21] J. Li, S. Chen, Z. Han, X. Qu, M. Jin, L. Deng, Q. Liang, Y. Jia, H. Wang, *Adv. Funct. Mater.* **2023**, *33*, 2306509.
[22] Z. Ji, Z. Li, L. Liu, Y. Zou, C.-A. Di, D. Zhu, *Adv. Mater. Technol.* **2024**, *9*, 2302128.
[23] L. Deng, Y. Liu, Y. Zhang, S. Wang, P. Gao, *Adv. Funct. Mater.* **2023**, *33*, 2210770.
[24] I. H. Eryilmaz, Y.-F. Chen, G. Mattana, E. Orgiu, *Chem. Commun.* **2023**, *59*, 3160.
[25] M. Lindorf, K. Mazzio, J. Pflaum, K. Nielsch, W. Brütting, M. Albrecht, *J. Mater. Chem. A* **2020**, *8*, 7495.
[26] S. Masoumi, S. O'Shaughnessy, A. Pakdel, *Nano Energy* **2022**, *92*, 106774.

[27] A. Tripathi, Y. Lee, S. Lee, H. Y. Woo, *J. Mater. Chem. C* **2022**, *10*, 6114.
[28] J. Wang, L. Liu, F. Wu, Z. Liu, Z. Fan, L. Chen, Y. Chen, *ChemSusChem* **2022**, *15*, 202102420.
[29] Y. J. Zeng, D. Wu, X. H. Cao, W. X. Zhou, L. M. Tang, K. Q. Chen, *Adv. Funct. Mater.* **2020**, *30*, 1903873.
[30] D. Zhou, H. Zhang, H. Zheng, Z. Xu, H. Xu, H. Guo, P. Li, Y. Tong, B. Hu, L. Chen, *Small* **2022**, *18*, 2200679.
[31] X. Rodríguez-Martínez, F. Saiz, B. Dörling, S. Marina, J. Guo, K. Xu, H. Chen, J. Martin, I. McCulloch, R. Rurali, *Adv. Energy Mater.* **2024**, *14*, 2401705.
[32] A. D. Scaccabarozzi, A. Basu, F. Aniés, J. Liu, O. Zapata-Arteaga, R. Warren, Y. Firdaus, M. I. Nugraha, Y. Lin, M. Campoy-Quiles, *Chem. Rev.* **2021**, *122*, 4420.
[33] J. Tang, Y.-H. Pai, Z. Liang, *ACS Energy Lett.* **2022**, *7*, 4299.
[34] D. Wang, H. Yu, W. Shi, C. Xu, *ACC Chem. Res.* **2023**, *56*, 2127.
[35] W. Zhao, J. Ding, Y. Zou, C.-A. Di, D. Zhu, *Chem. Soc. Rev.* **2020**, *49*, 7210.
[36] Y. Chang, Y.-H. Huang, P.-S. Lin, S.-H. Hong, S.-H. Tung, C.-L. Liu, *ACS Appl. Mater. Interfaces* **2024**, *16*, 3764.
[37] J. Song, H. Lu, M. Liu, H. Hu, J. Jiang, L. Zhang, H. Li, *Small* **2024**, *20*, 2308595.
[38] S. Wang, W. Zhu, I. E. Jacobs, W. A. Wood, Z. Wang, S. Manikandan, J. W. Andreasen, H. I. Un, S. Ursel, S. Peralta, *Adv. Mater.* **2024**, *36*, 2314062.
[39] R. Wu, W. Yu, X. Dai, L. Yan, W. Liu, D. Yuan, J. Zhu, X. Zhu, *Angew. Chem., Int. Ed.* **2024**, *64*, 202413061.
[40] X. Geng, T. Du, C. Xu, Y. Liu, Y. Deng, Y. Geng, *Adv. Funct. Mater.* **2023**, *33*, 2300809.
[41] J.-F. Ding, G.-L. Chen, P.-H. Liu, K.-W. Tseng, W.-N. Wu, J.-M. Lin, S.-H. Tung, L. Wang, C.-L. Liu, *J. Mater. Chem. A* **2024**, *12*, 9806.
[42] E. H. Suh, M. K. Jeong, K. Lee, W. Jeong, J. Jang, I. H. Jung, *Int. J. Energy Res.* **2021**, *45*, 21540.
[43] Z. Liu, Y. Hu, P. Li, J. Wen, J. He, X. Gao, *J. Mater. Chem. C* **2020**, *8*, 10859.
[44] I. E. Jacobs, Y. Lin, Y. Huang, X. Ren, D. Simatos, C. Chen, D. Tjhe, M. Statz, L. Lai, P. A. Finn, *Adv. Mater.* **2022**, *34*, 2102988.
[45] T. S. Lee, S. B. Lee, D.-Y. Choi, E. H. Suh, T. K. An, Y. J. Jeong, J. Jang, Y.-H. Kim, *Macromol. Res.* **2021**, *29*, 887.
[46] Z. Liang, Y. Zhang, M. Souri, X. Luo, A. M. Boehm, R. Li, Y. Zhang, T. Wang, D.-Y. Kim, J. Mei, *J. Mater. Chem. A* **2018**, *6*, 16495.
[47] J. Min, J. Im, S. H. Kim, H. H. Choi, K. Cho, *Adv. Funct. Mater.* **2023**, *33*, 2212825.
[48] Z. Ren, Z. Chen, Z. Luo, F. Zhong, Y. Wu, L. Jiang, Y. Chen, C. Gao, L. Wang, *ACS Appl. Mater. Interfaces* **2024**, *16*, 52988.
[49] H. Zeng, M. Mohammed, V. Untilova, O. Boyron, N. Berton, P. Limelette, B. Schmaltz, M. Brinkmann, *Adv. Electron. Mater.* **2021**, *7*, 2000880.
[50] Q. Zhou, C. Zhan, W. Wang, C. Li, D. Dong, S. Xiao, *ACS Appl. Polym. Mater.* **2023**, *6*, 277.
[51] J. Podlesný, O. Pytela, M. Klikar, V. Jelínková, I. V. Kityk, K. Ozga, J. Jedryka, M. Rudysh, F. Bureš, *Org. Biomol. Chem.* **2019**, *17*, 3623.
[52] D. Fichou, G. Horowitz, F. Garnier, *Synth. Met.* **1990**, *39*, 125.
[53] S. A. Gregory, R. Hanus, A. Atassi, J. M. Rinehart, J. P. Wooding, A. K. Menon, M. D. Losego, G. J. Snyder, S. K. Yee, *Nat. Mater.* **2021**, *20*, 1414.
[54] E. L. Ratcliff, J. L. Jenkins, K. Nebesny, N. R. Armstrong, *Chem. Mater.* **2008**, *20*, 5796.
[55] B. Wegner, D. Lungwitz, A. E. Mansour, C. E. Tait, N. Tanaka, T. Zhai, S. Duhm, M. Forster, J. Behrends, Y. Shoji, A. Opitz, U. Scherf, E. J. W. List-Kratochvil, T. Fukushima, N. Koch, *Adv. Sci.* **2020**, *7*, 2001322.
[56] R. C. Shallcross, T. Stubhan, E. L. Ratcliff, A. Kahn, C. J. Brabec, N. R. Armstrong, *J. Phys. Chem. Lett.* **2015**, *6*, 1303.
[57] A. Weathers, Z. U. Khan, R. Brooke, D. Evans, M. T. Pettes, J. W. Andreasen, X. Crispin, L. Shi, *Adv. Mater.* **2015**, *27*, 2101.
[58] J. Liu, X. Wang, D. Li, N. E. Coates, R. A. Segalman, D. G. Cahill, *Macromolecules* **2015**, *48*, 585.
[59] O. Zapata-Arteaga, A. Perevedentsev, S. Marina, J. Martin, J. S. Reparaz, M. Campoy-Quiles, *ACS Energy Lett.* **2020**, *5*, 2972.
[60] J. Kim, E. H. Suh, K. Lee, G. Kim, H. Kim, J. Jang, I. H. Jung, *Nanomaterials* **2023**, *13*, 1286.
[61] T. S. Lee, S. Nam, J. G. Oh, E. H. Suh, J. Jung, H. Oh, Y. J. Jeong, J. Jang, *Chem. Eng. J.* **2023**, *455*, 140925.
[62] E. H. Suh, M. K. Jeong, K. Lee, W. Jeong, Y. J. Jeong, I. H. Jung, J. Jang, *Adv. Funct. Mater.* **2022**, *32*, 2207886.
[63] E. H. Suh, J. G. Oh, J. Jung, S. H. Noh, T. S. Lee, J. Jang, *Adv. Energy Mater.* **2020**, *10*, 2002521.
[64] J. H. Park, Y. G. Seo, D. H. Yoon, Y.-S. Lee, S.-H. Lee, M. Pyo, K. Zong, *Euro. Polym. J.* **2010**, *46*, 1790.